

# Pressure-driven flow in a channel with porous walls\*

QIANLONG LIU<sup>1</sup> AND ANDREA PROSPERETTI<sup>1,2†</sup>

<sup>1</sup>Department of Mechanical Engineering, Johns Hopkins University, Baltimore MD 21218, USA

<sup>2</sup>Faculty of Science & Technology and Burgerscentrum, University of Twente, AE 7500 Enschede,  
The Netherlands

(Received 27 June 2010; revised 26 December 2010; accepted 8 March 2011;  
first published online 4 May 2011)

The finite-Reynolds-number three-dimensional flow in a channel bounded by one and two parallel porous walls is studied numerically. The porous medium is modelled by spheres in a simple cubic arrangement. Detailed results on the flow structure and the hydrodynamic forces and couple acting on the sphere layer bounding the porous medium are reported and their dependence on the Reynolds number illustrated. It is shown that, at finite Reynolds numbers, a lift force acts on the spheres, which may be expected to contribute to the mobilization of bottom sediments. The results for the slip velocity at the surface of the porous layers are compared with the phenomenological Beavers–Joseph model. It is found that the values of the slip coefficient for pressure-driven and shear-driven flow are somewhat different, and also depend on the Reynolds number. A modification of the relation is suggested to deal with these features. The Appendix provides an alternative derivation of this modified relation.

**Key words:** particle/fluid flow, sediment transport

---

## 1. Introduction

The flow over the surface of a fluid-saturated porous medium is encountered in a variety of important situations such as the bottom of water bodies (see e.g. Ouriemi, Aussillous & Guazzelli 2009; Seminara 2010), cracks in liquid-permeated rocks (see e.g. Koplik, Levine & Zee 1983; Popov, Efendiev & Qin 2009), irrigation (see e.g. Furman 2008), filtration (see e.g. Hanspal *et al.* 2006), material processing (see e.g. Le Bars & Worster 2006), biological interfaces (see e.g. Khakpour & Vafai 2008) and many others.

While Darcy's law is commonly used to describe the flow in the bulk of the porous medium, there is no unique prescription on how to join the Darcy velocity to the unobstructed flow on the other side of the porous medium interface. The well-known Brinkman equation augments Darcy's law by a viscous term similar to the one present in the Navier–Stokes momentum equation, which permits a smooth transition across the interface (see e.g. Neale & Nader 1974; Vafai & Kim 1990; Alazmi & Vafai 2001; Le Bars & Worster 2006; Nield & Kuznetsov 2009). However, questions arise as to the proper viscosity parameter to use in the Brinkman model (see e.g. Koplik

\* With an appendix by Daniel Lhuillier

† Email address for correspondence: prosperetti@jhu.edu

*et al.* 1983; Martys, Bentz & Garboczi 1994; Goyeau *et al.* 2003; Le Bars & Worster 2006) and, furthermore, the predicted length scale for the penetration of the flow into the porous medium is found to be at variance with the available data (see e.g. Goharzadeh, Khalili & Jørgensen 2005; Ghisalberti 2009; Morad & Khalili 2009; Pokrajac & Manes 2009).

A different approach was initiated by Beavers & Joseph (1967) (see also Nield 2009) who postulated an interface relation of the form

$$\left. \frac{dU}{dz} \right|_{z=0^+} = \frac{\alpha}{\sqrt{\kappa}} (U_i - U_D), \quad (1.1)$$

where  $U = U(z)$  is the mean velocity in the flow direction  $x$ ,  $U_i$  is the slip velocity at the porous medium interface  $z=0$ ,  $\kappa$  is the permeability and  $\alpha$  is a phenomenological dimensionless parameter. The Darcy velocity  $U_D$ , which represents the mean flow rate per unit area in the bulk of the porous medium, is given by

$$U_D = -\frac{\kappa}{\mu} \frac{dP}{dx}, \quad (1.2)$$

in which  $dP/dx$  is an imposed mean pressure gradient and  $\mu$  is the fluid viscosity. In this picture, on traversing the interface, the velocity undergoes a discontinuity from  $U_D$  to  $U_i$ . The literature contains several derivations of the Beavers–Joseph relation based on various forms of averaging (see e.g. Saffman 1971; Ochoa-Tapia & Whitaker 1995), homogenization (see e.g. Auriault 1991; Cieszko & Kubik 1999; Jäger & Mikelić 2009) and others (see e.g. Chandesris & Jamet 2009; Valdés-Parada *et al.* 2009).

Much of this work relies on a variety of hypotheses and assumptions which, while eminently plausible, it has proven difficult to scrutinize in detail. The early experimental work, such as the original one of Beavers & Joseph (1967) and related subsequent studies, gave only indirect evidence as to the nature of the interfacial phenomena. More recent attempts, such as those of Goharzadeh *et al.* (2005), Morad & Khalili (2009) and Pokrajac & Manes (2009), have difficulties resolving the flow very near the porous medium interface. Analytical work is limited to somewhat artificial situations (see e.g. Richardson 1971; Taylor 1971) or relatively high porosities (see e.g. James & Davis 2001). Numerical simulations have been carried out in the Stokes regime (Larson & Higdon 1987), for flow over banks of cylinders (Sahraoui & Kaviany 1992; Zhang & Prosperetti 2009) and for arrays of cubes (Breugem, Boersma & Uittenbogaard 2005; Chandesris & Jamet 2009; Valdés-Parada *et al.* 2009).

The purpose of the present paper is to describe the results of finite-Reynolds-number numerical simulations over a model porous medium made of spheres arranged in a simple cubic pattern (figure 1). We first describe several features of the flow and calculate forces and torque on the spheres. In particular, we find a non-zero lift force on the particles in the top layer of the porous medium which may play a role on the transport of bottom sediments. Then we examine the Beavers–Joseph relation (1.1) and find that the coefficient  $\alpha$  necessary to describe the simulation results is different for pressure-driven and shear-driven conditions, and depends on the Reynolds number. We had already found an indication of these features in an earlier study of the flow over a cylinder bank (Zhang & Prosperetti 2009), but here the analysis is carried out for the more realistic three-dimensional case and is more detailed. A modified relation capable of accounting for both situations is introduced. We also quantify the requirement of scale separation postulated in earlier theoretical

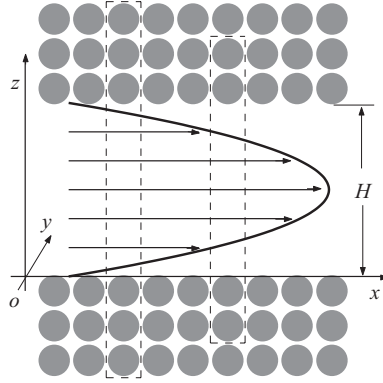


FIGURE 1. The situation studied in this paper. The two computational domains used are shown by the dashed area; periodicity is assumed along the three coordinate directions.

studies of the interfacial phenomena finding that it is more readily met in shear than in pressure-driven flow and, in both cases, it is less stringent than might be expected *a priori*.

## 2. Mathematical model

The flow situation we consider is shown in figure 1, where the dashed lines show the two domains used in the computations. The conditions at the boundaries of these domains enforce a triple periodicity in space, with the spheres arranged in simple cubic lattices. In the main flow direction  $x$  and in the direction  $y$  normal to the page, the spatial period is  $L = 2(a + \delta)$ , where  $a$  is the sphere radius and  $2\delta$  is the minimum gap between two adjacent spheres. In the vertical direction  $z$  the period is  $N_s L + H - 2\delta$  where  $N_s = 4$  or  $6$  is the number of spheres stacked vertically in the computational domain (see dashed lines in figure 1). The correction  $2\delta$  accounts for the fact that the clear-channel width  $H$  includes part of the cell corresponding to the two spheres facing it (see figure 1). If we define the bulk sphere volume fraction by

$$\beta = \frac{\frac{4}{3}\pi a^3}{L^3}, \quad (2.1)$$

one easily deduces that

$$\frac{\delta}{L} = \frac{1}{2} - \frac{a}{L} = \frac{1}{2} - \left(\frac{3\beta}{4\pi}\right)^{1/3}. \quad (2.2)$$

As will be shown later, the flow is essentially triply periodic with period  $L$  already one sphere layer away from the unobstructed channel so that, in effect, even such a small number of spheres is already sufficient to simulate infinite porous media.

We solve the incompressible Navier–Stokes equations

$$\nabla \cdot \mathbf{u} = 0, \quad (2.3)$$

$$\frac{\partial \mathbf{u}}{\partial t} + \mathbf{u} \cdot \nabla \mathbf{u} = -\frac{1}{\rho} \nabla p + \nu \nabla^2 \mathbf{u} + G \mathbf{i}. \quad (2.4)$$

Here,  $\mathbf{u}$  and  $p$  are the velocity and perturbation pressure fields,  $\rho$  and  $\nu = \mu/\rho$  are the fluid density and kinematic viscosity,  $\mathbf{i}$  is a unit vector in the main flow direction

$x$  and

$$G = -\frac{1}{\rho} \frac{dP}{dx} \quad (2.5)$$

is the acceleration caused by the imposed mean pressure gradient. This system is solved imposing on all the variables the same spatial periodicity as that of the unit cell; on the faces of the cell parallel to the main flow direction, the normal velocity components are set to 0. We solve the initial-value problem, but all the results presented in this paper are for steady-state conditions.

### 3. Velocity scales

There are several velocity and length scales in the problem, each one of which is appropriate to describe a different aspect of the flow.

The mean flow rate in a plane channel bounded by two parallel no-slip plates separated by a distance  $H$  is related to the imposed pressure gradient  $-\rho G$  by

$$U_m = \frac{H^2 G}{12\nu}. \quad (3.1)$$

With this velocity scale we can define a Reynolds number  $Re_H$  for flow in the unobstructed channel by

$$Re_H = \frac{H U_m}{\nu} = \frac{H^3 G}{12\nu^2}. \quad (3.2)$$

In order to obtain an estimate of the slip velocity  $U_i$  appearing in the Beavers–Joseph relation (1.1), we take  $\alpha = 1$ , neglect  $U_D$  and use the standard Poiseuille result for  $dU/dz$ , which is independent of wall slip; the result is

$$U_* = \frac{H G \sqrt{\kappa}}{2\nu}. \quad (3.3)$$

The particles in the sphere layer facing the channel are subjected to a velocity of this order of magnitude, which permits us to define a particle Reynolds number  $Re_p$  by

$$Re_p = \frac{2a U_*}{\nu} = \frac{a H \sqrt{\kappa} G}{\nu^2}. \quad (3.4)$$

From these expressions we readily find that

$$\frac{U_*}{U_m} = 3 \frac{U_D}{U_*} = 6 \frac{\sqrt{\kappa}}{H}, \quad (3.5)$$

which shows that, since  $\sqrt{\kappa}$  must be smaller than  $H$  for an average treatment to be justified, one usually has  $U_D \ll U_* \ll U_m$ .

The velocity  $U_*$  represents only an estimate of the velocity at the interface. The more precise estimate of  $U_i$  which we obtain from the numerical simulations permits us to define an interfacial Reynolds number  $Re_i$  from

$$Re_i = \frac{2a U_i}{\nu}. \quad (3.6)$$

Since  $Re_i/Re_p = U_i/U_*$ , this ratio may be expected to be a number close to 1.

### 4. Forces

We will show results for the force and couple on the spheres in the top layer. For the former, an appropriate scale  $F_*$  is the shear stress at the interface,  $\tau_w \simeq \mu dU/dz|_{z=0+}$

multiplied by a measure of the particle area,  $\pi a^2$ . For the couple, the appropriate scale  $T_*$  is the scale for the force multiplied by the particle radius  $a$ . Thus, we define

$$F_* = \frac{\pi}{2} \rho G a^2 H, \quad T_* = \frac{\pi}{2} \rho G a^3 H. \quad (4.1)$$

If the momentum equation (2.4) is integrated over the computational domain of volume  $V$ , using incompressibility, periodicity, the no-slip condition and the divergence theorem, one readily finds

$$\frac{d}{dt} \rho \oint_V \mathbf{x}(\mathbf{u} \cdot \mathbf{n}) dS = \sum_{j=1}^{N_s} \mathbf{F}_j - V(1 - \beta) \rho G \mathbf{i}, \quad (4.2)$$

in which

$$\mathbf{F}_j = \oint_{S_j} (-p \mathbf{n} + \boldsymbol{\tau} \cdot \mathbf{n}) dS_j, \quad (4.3)$$

with  $\boldsymbol{\tau}$  the viscous stress tensor and  $\mathbf{n}$  the outer normal, is the hydrodynamic force on the  $j$ th sphere. Because of the incompressibility condition, the integral in the left-hand side is independent of the position of the point from which the position vector  $\mathbf{x}$  is measured and, by the definition of the particle volume fraction  $\beta$ ,  $V(1 - \beta)$  is the total volume of fluid in the computational domain. The cross-stream components of (4.2) simply reduce to

$$\sum_{j=1}^{N_s} F_{j,y} = \sum_{j=1}^{N_s} F_{j,z} = 0, \quad (4.4)$$

while, for steady flow, the  $x$ -component is

$$\frac{1}{V} \sum_{j=1}^{N_s} F_{j,x} = (1 - \beta) \rho G. \quad (4.5)$$

A similar argument applied to a cell of volume  $L^3$  of an infinite porous medium modelled as spheres in a simple cubic arrangement gives

$$K \equiv \frac{F_{x,porous}}{6\pi\mu U_D} = \frac{(1 - \beta)L^3}{6\pi a \kappa}. \quad (4.6)$$

Upon using (2.1), this relation gives the following expression for the so-called Darcy number  $\kappa/a^2$ :

$$\frac{\kappa}{a^2} = \frac{2}{9} \frac{1 - \beta}{\beta K}. \quad (4.7)$$

Relations (4.4), (4.5) and (4.7) will be useful to test the numerical accuracy of our method as shown in the next section.

## 5. Numerical method and validation

As in our previous paper (Zhang & Prosperetti 2009), our numerical simulations are carried out using the PHYSALIS method which, for the present three-dimensional situation, is described in detail in Zhang & Prosperetti (2005). The method is essentially of the immersed boundary type, with an important twist. Due to the no-slip condition, *in the immediate neighbourhood* of each particle, the Navier–Stokes equations can be accurately approximated by the linearized Stokes equations whatever

$\beta$	Sangani & Acrivos	Present	% difference	$a/\Delta x$	$N_t$
0.3508	0.03897	0.03990	2.39	14	3
0.3508	0.03897	0.03960	1.62	14	4
0.3030	0.05957	0.06038	1.36	10	3
0.3030	0.05957	0.06009	0.873	10	4
0.2464	0.1016	0.1012	0.415	14	3
0.2209	0.1314	0.1325	0.900	6	3
0.2209	0.1314	0.1320	0.487	12	3
0.1908	0.1814	0.1820	0.287	10	3
0.1131	0.4945	0.4953	0.171	6	3

TABLE 1. Comparison of the present results for the dimensionless force (4.6) with those of Sangani & Acrivos (1982).

the Reynolds number. For example, it was shown in Zhang & Prosperetti (2005) that, even at a Reynolds number of 50, the Stokes approximation is accurate up to distances of 10 % of the particle radius and beyond. As the Reynolds number increases, the region where this approximation is applicable shrinks, but is never zero.

For spheres, the Stokes solution can be expressed in analytic form as a superposition of modes containing undetermined coefficients, which are calculated by matching the local analytic solution with a finite difference solution away from the particles. The latter is calculated by a standard first-order projection method. A notable feature of the method is that the no-slip condition at the surface of the spheres is satisfied exactly and the first few coefficients of the expansion directly give the hydrodynamic force and couple on the spheres, avoiding the need to integrate the fluid stress over their surface.

In order to increase the accuracy of the method, in this work the part of the flow domain containing particles was discretized with a grid finer by a factor of 2 in each direction with respect to the grid used elsewhere in the computational domain similarly to an earlier paper (Liu & Prosperetti 2010). Matching between the Stokes solution and the finite-difference solution was carried out at the nodes adjacent to the particle surface, i.e. at a distance from the surface of at most about one fine-mesh length. The fine grid extended at least eight small cells into the unobstructed flow region.

Just as in the cylinder case of our earlier paper (Zhang & Prosperetti 2009), and as shown below, we found that the flow below the outer sphere layer was essentially independent of distance from the clear fluid region and therefore behaved like the flow in an infinitely periodic porous medium with a cubic fundamental cell of side  $L$  and a sphere volume fraction given by (2.1). This observation permits us to validate the calculation by comparing the permeability resulting from our calculation with that reported in the literature.

Sangani & Acrivos (1982) and Zick & Homsy (1982) have calculated the dimensionless force  $K$  defined in (4.6) as a function of the volume fraction  $\beta$  for Stokes flow. Although here we solve the full Navier–Stokes equations, for small pressure gradients the effect of inertia is so small as to be negligible. We compare our results with Sangani & Acrivos’s in table 1 for  $a^3G/\nu^2 = 0.01$ . Here  $\Delta x$  is the mesh size of the fine grid surrounding the particles and  $N_t$  is the order of truncation of the infinite series representing the local Stokes-flow solution near the spheres. Note that  $N_t = 3$  corresponds to retaining a total of 46 coefficients while, with  $N_t = 4$ , 73 coefficients are retained.

$a^3 G/\nu^2$	$Re$	$\frac{\sum_{j=1}^{N_s} F_{x,j}}{\rho(1-\beta)GV}$	$\frac{\sum_{j=1}^{N_s} F_{y,j}}{\rho(1-\beta)GV}$	$\frac{\sum_{j=1}^{N_s} F_{z,j}}{\rho(1-\beta)GV}$
0.001	0.0833	0.9916	$1.337 \times 10^{-7}$	$-2.651 \times 10^{-10}$
0.01	0.833	0.9916	$1.337 \times 10^{-6}$	$-2.273 \times 10^{-9}$
0.1	8.33	0.9916	$1.331 \times 10^{-5}$	$-2.273 \times 10^{-8}$
1	83.3	0.9916	$-1.415 \times 10^{-4}$	$9.825 \times 10^{-5}$
5	417	0.9929	$-1.886 \times 10^{-4}$	$2.871 \times 10^{-5}$
10	833	0.9929	$-6.188 \times 10^{-6}$	$-9.973 \times 10^{-5}$

TABLE 2. Comparison of the numerical results with the exact relations (4.4) and (4.5). For this calculation  $\beta = 0.303$  and  $H/a = 10$ ;  $G$  is the imposed pressure gradient.

Another test can be conducted at finite Reynolds number by examining the accuracy with which the force relations (4.4) and (4.5) are verified. Some results are shown in table 2 for different  $G$  with  $\beta = 0.303$  and  $H/a = 10$ . These results have been calculated with  $N_t = 3$ . We did some tests with  $N_t = 4$ , finding differences of the order of a small fraction of 1 %. Similarly, we have found that the difference between the computed force in the flow direction and the expression (7.1) shown below was less than 1 %.

The results of these tests indicate convergence as the mesh is refined and the number of coefficients increased. The results shown below have been obtained with  $N_t = 3$  and between 7 and 10 fine-grid mesh lengths per sphere radius.

As the particle volume fraction increases the spheres get closer and closer, which requires the use of a progressively finer mesh in the gaps between them and of many more terms in the analytic Stokes solution. In order to maintain the computational load reasonable, it would be necessary to use different grids inside and near the porous medium and in the channel. This flexibility is not yet implemented in our code. Thus, in this paper, we limit ourselves to relatively high porosities with a maximum particle volume fraction of about 30 %.

## 6. Flow field

With the simple cubic sphere arrangement specified, there are only three independent dimensionless parameters for the problem as specified. We take them to be the particle volume fraction, the dimensionless channel height and the dimensionless imposed pressure gradient:

$$\beta, \quad \frac{H}{a}, \quad \frac{a^3 G}{\nu^2}. \quad (6.1)$$

The channel and particle Reynolds numbers  $Re_H$  and  $Re_p$  are related to the dimensionless channel height, permeability and pressure gradient by

$$Re_H = \frac{1}{12} \left( \frac{H}{a} \right)^3 \frac{a^3 G}{\nu^2}, \quad Re_p = \frac{\sqrt{\kappa}}{a} \frac{H}{a} \frac{a^3 G}{\nu^2}. \quad (6.2)$$

We begin our description of the flow field by showing in figures 2–4 several sections of the stream surfaces in the region between two consecutive spheres in the top layer facing the unobstructed channel. The channel height is  $H/a = 10$ , the dimensionless

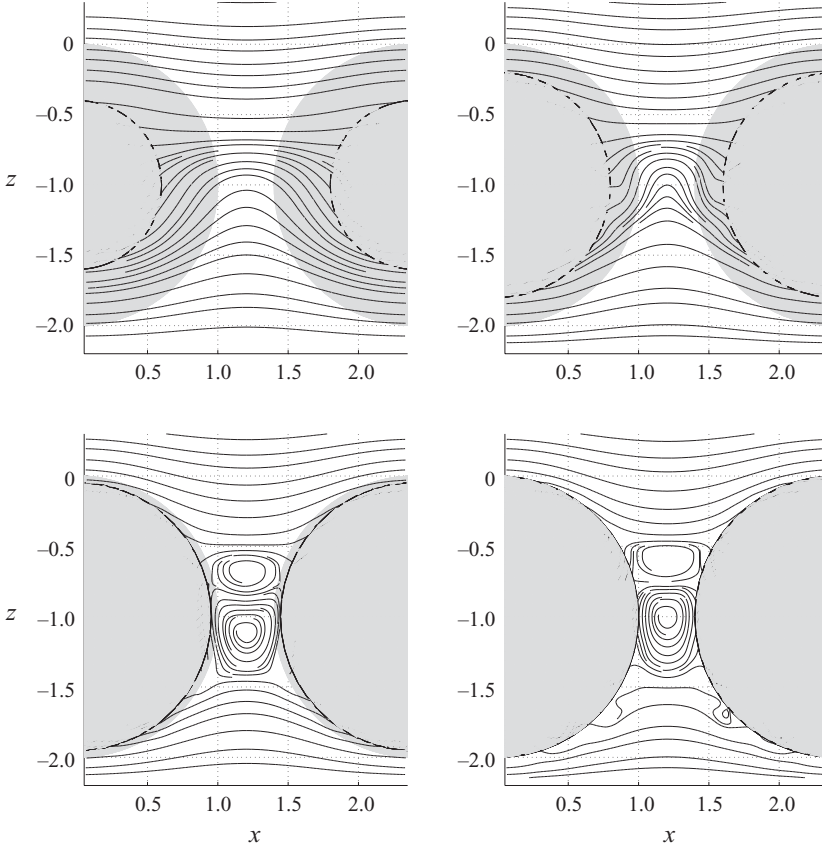


FIGURE 2. Traces of the stream surfaces on  $y = \text{const.}$  planes (see figure 1) in the neighbourhood of the top sphere layer; the dashed circles mark the intersection of the planes with the sphere. The sections are taken at distances  $0.8a$ ,  $0.6a$ ,  $0.3a$  and  $0$  from the sphere centre for  $a^3G/\nu^2 = 0.01$ ,  $\beta = 0.303$ ,  $H/a = 10$ . The channel, interfacial and particle Reynolds numbers have the values  $Re_H = 0.833$ ,  $Re_i = 0.0297$  and  $Re_p = 0.0244$ .

pressure gradients are  $a^3G/\nu^2 = 0.01$ ,  $1$  and  $10$ , respectively, and the corresponding Reynolds numbers  $Re_H = 0.833$ ,  $83.3$  and  $833$ . Here  $L/a = 2.4$ , which corresponds to a sphere volume fraction  $\beta \simeq 0.303$  in the bulk of the porous medium.

The sections are with  $y = \text{const.}$  planes (see figure 1) at distances  $0.8a$ ,  $0.5a$ ,  $0.3a$  and  $0$  from the sphere centre; the plane  $y = 0$  is the plane of symmetry through the sphere centre. In the figures the entire sphere is shaded, but the diameter of the circle cut by the plane of the figure is evident from the points where stream surfaces begin and end. In interpreting these figures it should be kept in mind that only the cut with the symmetry planes (last panel in each group) shows actual streamlines; the other images show cuts of the stream surfaces. The small irregularities near the sphere surfaces are artefacts of the plotting subroutine and should be disregarded.

For the very small pressure gradient  $a^3G/\nu^2 = 0.01$  (figure 2), corresponding to  $Re_H = 0.833$  and  $Re_p = 0.0244$ , the streamlines on the symmetry midplane and the neighbouring stream surfaces show vortices with upstream/downstream symmetry as expected. These structures are similar to those of the two-dimensional case of Zhang & Prosperetti (2009). The outermost cut at  $0.8a$ , which is farthest from the centre, shows an open loop similar to the two-dimensional results at small volume



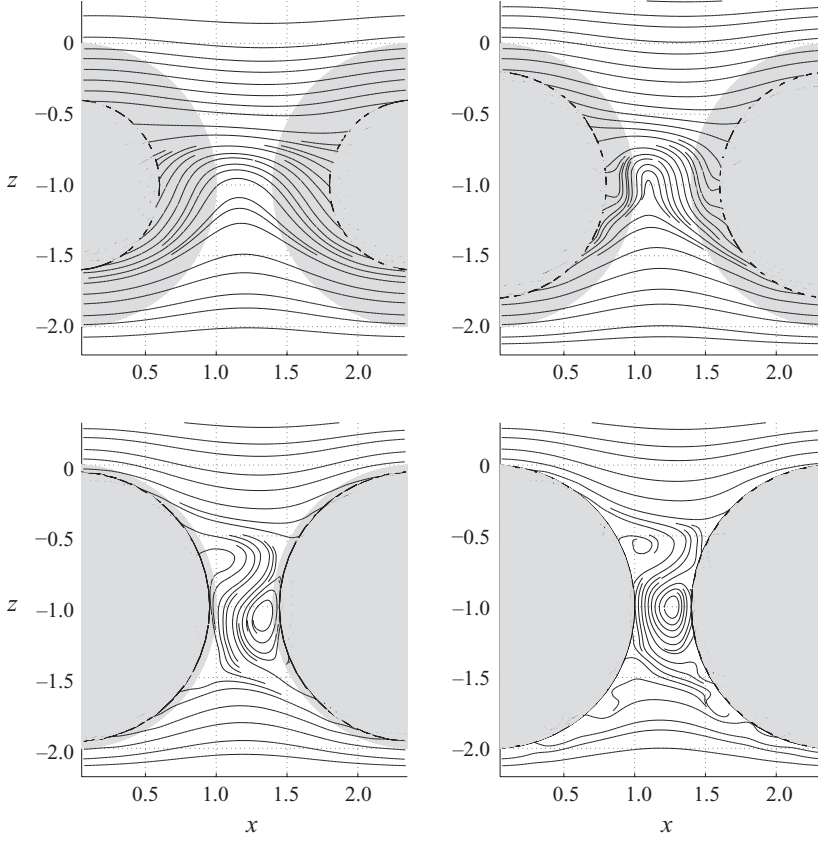


FIGURE 3. Traces of the stream surfaces on  $y = \text{const.}$  planes (see figure 1) in the neighbourhood of the top sphere layer; the dashed circles mark the intersection of the planes with the sphere. The sections are taken at distances  $0.8a$ ,  $0.6a$ ,  $0.3a$  and  $0$  from the sphere centre for  $a^3G/\nu^2 = 1$ ,  $\beta = 0.303$ ,  $H/a = 10$ . The channel, interfacial and particle Reynolds numbers have the values  $Re_H = 83.3$ ,  $Re_i = 2.93$  and  $Re_p = 2.44$ .

fraction. It is as if the curvature of the flow in the direction normal to the page is not a very significant feature and the flow essentially responds to the obstructed area fraction in the plane of the cut in a quasi-two-dimensional fashion.

The situation is different at the higher Reynolds numbers. A marked upstream/downstream asymmetry is evident already for a pressure gradient  $a^3G/\nu^2 = 1$ , for which  $Re_H = 83.3$  and  $Re_p = 2.44$  (figure 3). There is a clear streamline/stream surface separation from the upstream sphere and reattachment to the downstream one. The stagnation point on the symmetry plane on the downstream sphere has a three-dimensional nature, so that the flow is not simply deflected up or down as in the two-dimensional case, but also sideways. This circumstance confers to the flow structures in the gap a markedly different appearance from those found in the case of cylinders. These features are even more evident for  $a^3G/\nu^2 = 10$ , for which  $Re_H = 833$  and  $Re_p = 24.4$  (figure 4). One notices the presence of three-dimensional separation bubbles the axes of which approximately and partially follow ‘parallels’ on the sphere surfaces normal to the page. The general structure of these stream surfaces has similarities with those sketched in figure 7 of Pokrajac & Manes (2009). In particular, near the symmetry plane one observes similar closed streamlines in the

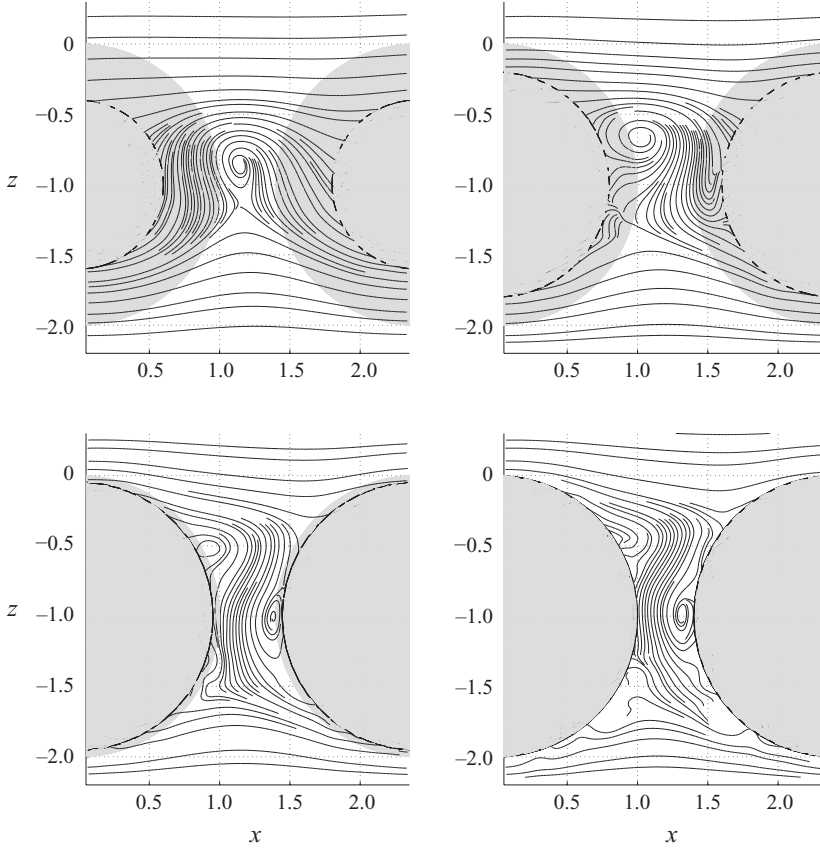


FIGURE 4. Traces of the stream surfaces on  $y = \text{const.}$  planes (see figure 1) in the neighbourhood of the top sphere layer; the dashed circles mark the intersection of the planes with the sphere. The sections are taken at distances  $0.8a$ ,  $0.6a$ ,  $0.3a$  and  $0$  from the sphere centres for  $a^3G/\nu^2 = 10$ ,  $\beta = 0.303$ ,  $H/a = 10$ . The channel, interfacial and particle Reynolds numbers have the values  $Re_H = 833$ ,  $Re_i = 26.7$  and  $Re_p = 24.4$ .

gap and a similar rise and fall of the streamlines in the cuts further removed from the plane of symmetry.

The pressure distributions on the plane of symmetry (figure 5) show high and low pressures near the points of reattachment and separation. In the figure the arbitrary pressure constant has been fixed by requiring the same pressure values at the point protruding the farthest into the unobstructed channel. The pressure distribution in excess of the mean surface value on the surface of the spheres is shown in figure 6. In this figure the topmost point of the sphere surface corresponds to  $\theta = 0$  and the lowest one to  $\theta = \pi$ . The mean flow is directed from  $\phi = \pi$  toward  $\phi = 0$  and the cross-stream direction runs from  $\phi = \frac{3}{2}\pi$  to  $\phi = \frac{1}{2}\pi$ . It may be noticed that, except for the low-Reynolds-number case  $a^3G/\nu^2 = 0.01$ , the maximum pressure is consistently smaller than the minimum and, furthermore, that the point of maximum pressure tends to be lower than that of minimum pressure. The combination of these two features contributes to a lift force on the spheres as will be seen later.

Models based on the Brinkman equation with the same viscosity as the pure fluid predict a depth of penetration of the unobstructed channel flow into the porous medium of the order of  $\sqrt{\kappa}$ , which here equals  $0.244a$  (see e.g. Le Bars & Worster

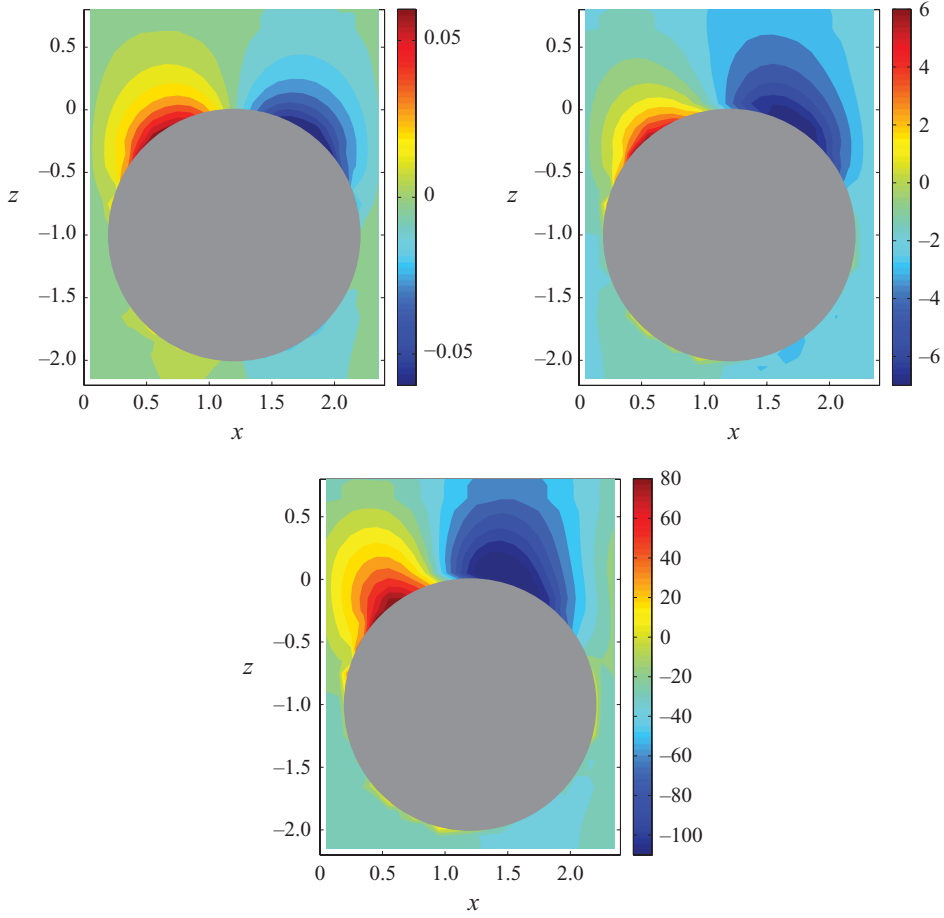


FIGURE 5. (Colour online available at [journals.cambridge.org/FLM](http://journals.cambridge.org/FLM)) Pressure distribution in the neighbourhood of the top sphere layer in the plane of symmetry through the sphere centres. The three panels are for  $a^3G/v^2 = 0.01, 1$  and  $10$ .

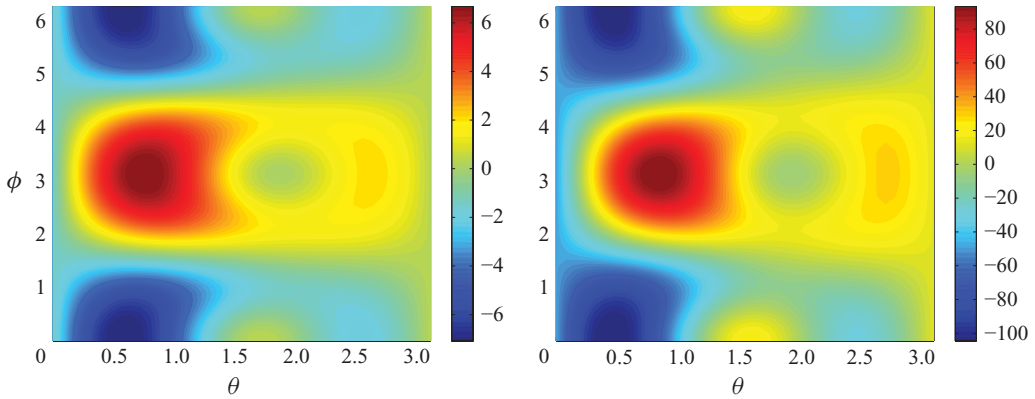


FIGURE 6. (Colour online) Pressure distribution over the surface of the spheres in the top layer for  $a^3G/v^2 = 1$  and  $10$ . The highest and lowest points of the sphere surface correspond to  $\theta = 0$  and  $\theta = \pi$ , the mean flow is directed from  $\phi = \pi$  toward  $\phi = 0$  and the cross-stream direction (increasing  $y$ , cf. figure 1) runs from  $\phi = \frac{3}{2}\pi$  to  $\phi = \frac{1}{2}\pi$ .

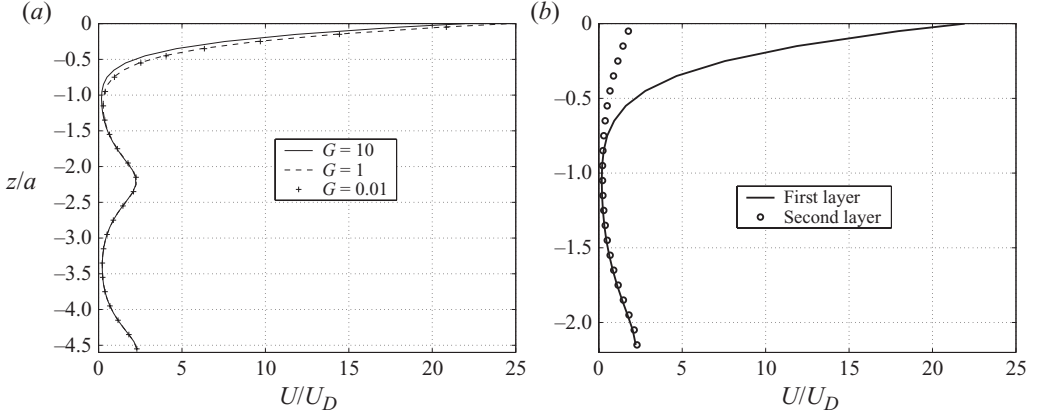


FIGURE 7. (a) Horizontally averaged velocity  $U(z)$  defined in (6.3) normalized by the Darcy velocity (1.2) for  $a^3 G / \nu^2 = 0.01$  (crosses), 1 (dashed line) and 10 (solid line) and  $\beta = 0.303$ . The plane  $z = 0$  is tangent to the topmost sphere surfaces. (b) The horizontally averaged velocity profile between the first and second sphere layers (circles) shifted upward for comparison with the profile in the first top layer for  $a^3 G / \nu^2 = 10$ .

2006; Tilton & Cortelezzi 2008; Nield 2009). Experiment suggests, on the other hand, that the relevant length scale is the particle size (Goharzadeh *et al.* 2005; Morad & Khalili 2009). The same conclusion was found in the two-dimensional case of Zhang & Prosperetti (2009). In order to examine this feature in the present situation, we study the depth dependence of the horizontally averaged  $x$ -velocity, namely

$$U(z) = \frac{1}{L^2} \int dx \int dy u_x(x, y, z). \quad (6.3)$$

The left panel of figure 7 is a graph of this quantity normalized by the Darcy velocity (1.2) for  $a^3 G / \nu^2 = 0.01$ , 1 and 10 and  $\beta = 0.303$ . For the reasons explained by Sahraoui & Kaviany (1992) and James & Davis (2001), we take the interface  $z = 0$  of the porous medium as the plane tangent to the topmost sphere layer and we denote the mean slip velocity on this plane by  $U_i = U(z = 0)$ . The sphere centres are at  $z/a = -1$  and  $z/a \simeq -3.4$ . For the three cases, the results between  $z = 0$  and  $z = -1$  are close and, to this extent, the Brinkman prediction may be considered verified. For a near-indistinguishability of the velocity distributions, however, which would imply the validity of Darcy's law, one has to go deeper, below the line of centres of the first sphere layer. We find that this depth is about four times the Brinkman prediction, which also implies a good match between our computations and experiment.

The average velocity distributions between the top and the next-to-the-top sphere also become virtually identical below the line of centres of the top sphere layer as shown in the right panel of figure 7 for  $a^3 G / \nu^2 = 10$ . The horizontal forces acting on the spheres in the second and third layers differ by less than 0.2 %. For these reasons, after the first tests in which we used three to four sphere layers to simulate each half of the porous medium, we conducted the rest of the simulations with only two as indicated by the rightmost dashed rectangle in figure 1.

While  $U_D$  is the proper velocity scale in the porous medium, the mean channel velocity  $U_m$  defined in (3.1) is the proper scale for the flow above it. Figure 8 shows  $U/U_m$  versus  $z$  for  $a^3 G / \nu^2 = 0.01$  and 10. The circles show the results of the numerical calculation and the solid lines are a parabolic fit which allows for slip at the plane

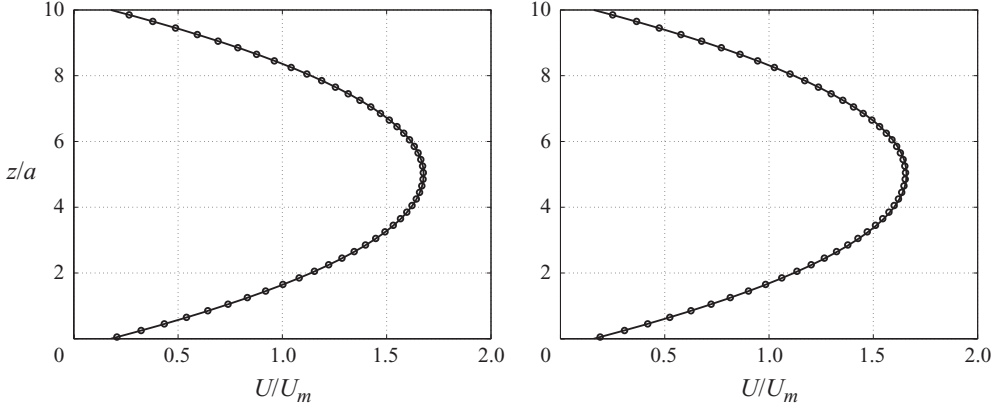


FIGURE 8. Distribution of the horizontally averaged velocity in the channel  $U(z)$  normalized by the Poiseuille mean velocity  $U_m$  defined in (3.1) for  $a^3 G / \nu^2 = 0.01$  and 10. The results of the numerical calculation are indicated by the circles, while the solid lines show a parabolic fit which allows for slip at the plane tangent to the spheres.

tangent to the spheres. It can be seen that this parabolic Poiseuille-like fit reproduces very well the mean velocity profile. We address the issue of slip at the porous medium surface later in § 8.

## 7. Force and torque on the outermost layer of spheres

We now consider the hydrodynamic forces and torques acting on the spheres in the top layer normalized by the quantity  $F_* \propto G$  defined in (4.1).

If the argument of § 4 is applied to a volume enclosing only two spheres symmetrically located with respect to the channel centre-plane, and the flow is assumed essentially periodic on the horizontal planes bounding this volume as suggested by figure 7, we find

$$F_{x, \text{surf. sphere}} = L^3 \left( \frac{H - 2\delta}{2L} + 1 - \beta \right) \rho G, \quad (7.1)$$

where  $\delta$  is defined in (2.2). We thus see that, with respect to the spheres in the bulk, the surface spheres are subjected to a larger drag force in the ratio

$$\frac{F_{x, \text{surf. sphere}}}{F_{x, \text{porous}}} = 1 + \frac{H - 2\delta}{2(1 - \beta)L}. \quad (7.2)$$

The solid line in figure 9 is the normalized lift force, namely the force in the vertical direction normal to the main flow, for  $\beta = 0.303$  and  $H/a = 10$ , as a function of the particle Reynolds number  $Re_p$  defined in (3.4). The pressure and viscous components of this total force are shown by the dashed and dash-dotted lines, respectively. The symbols show a few results for other values of  $\beta$  and  $H/a$  as explained in the figure caption. It can be seen that, once the lift force is plotted in this way, the dependence on these variables is rather weak, which implies that the scales used for the normalization adequately capture the main flow phenomena determining this quantity. The very slight dependence on the volume fraction indicates that this force is strongly dominated by the flow over the exposed surface of the sphere. This feature is in agreement with the fact that the viscous component is always smaller than the pressure component, even at low Reynolds numbers, and becomes progressively weaker. For

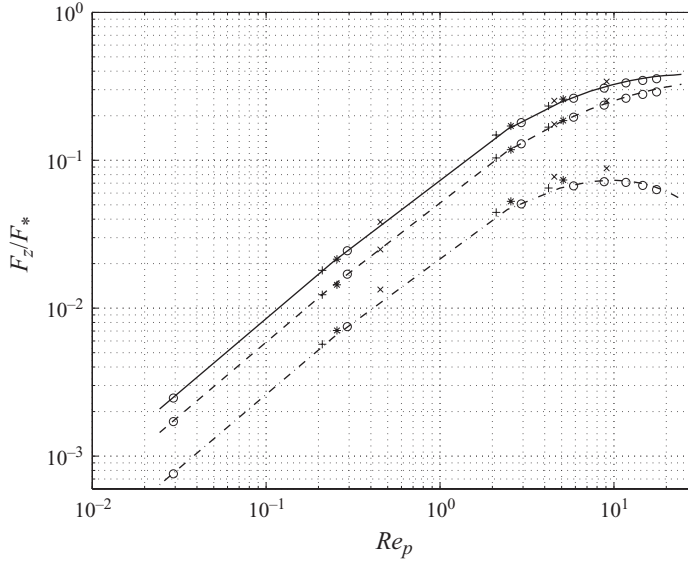


FIGURE 9. Normalized lift force on the spheres in the top layer of the porous medium as a function of the particle Reynolds number  $Re_p$  defined in (3.4). The solid line is the total force for  $\beta = 0.303$  and  $H/a = 10$ , while the dashed and dash-dotted lines are the pressure and viscous components, respectively. The circles are the results for  $\beta = 0.303$  with  $H/a = 12$ , the pluses and asterisks for  $\beta = 0.287$  and  $0.246$  with  $H/a = 8$  and the crosses for  $\beta = 0.180$  with  $H/a = 10$ .

small Reynolds numbers the lines have slope 1, implying that  $F_z \propto G^2$  as expected due to the reversibility of Stokes flow. As  $Re$  increases, the dimensionless force approaches a constant value implying a proportionality of  $F_z$  to the imposed pressure gradient  $G$ . This feature suggests that the proper pressure scale at the pore level is the viscous scale  $\mu U_D/a$  rather than the inertial scale  $\frac{1}{2}\rho U_D^2$ , which is not surprising given the importance of viscous effects near the spheres as well as the force relation (4.5). The same trends were found in the case of cylinders in Zhang & Prosperetti (2009).

Figure 10 shows the normalized couple acting on the spheres in the top layer as a function of  $Re_p$ . The solid line is for  $\beta = 0.303$  with  $H/a = 10$ , while the symbols are for several other values of  $\beta$  and  $H/a$  as explained in the caption. The couple decreases with increasing  $Re_p$  presumably in response to the increasing importance of flow separation. This behaviour is also consistent with the decrease of the angular velocity of a sphere suspended in a shear flow (see e.g. Lin, Peery & Schowalter 1970; Bagchi & Balachandar 2002). The results for  $H/a = 10$  (solid line) and  $H/a = 12$  (circles) are very close, indicating that for  $H/a \simeq 10$  the channel height ceases to influence the results. Contrary to the case of the lift force, we see here a greater dependence on the volume fraction which, however, remains weak. For example, the permeabilities for  $\beta = 0.180$  and  $\beta = 0.303$  differ by a factor of nearly 4, while the scaled couples differ by less than 20 %.

## 8. Effective slip at the porous medium interface

The present numerical results enable us to examine the phenomenological boundary condition (1.1). As noted in the Introduction, in spite of several attempts at a derivation, the precise status of this relation is still unclear.

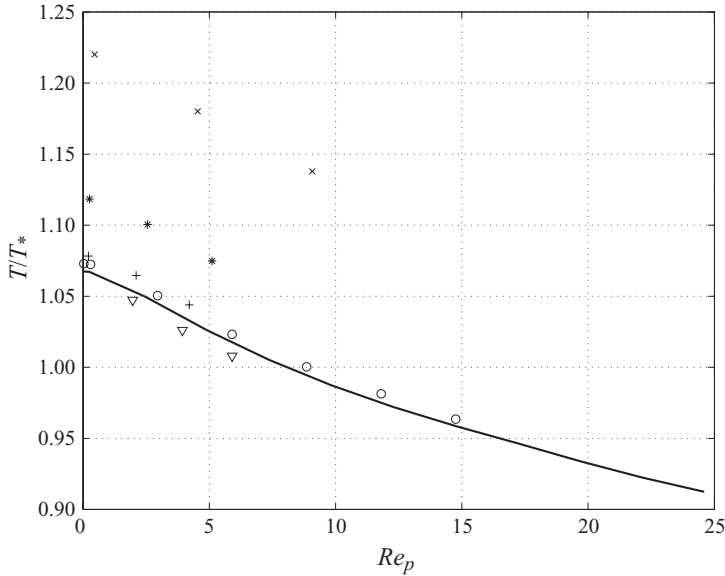


FIGURE 10. Normalized couple on the spheres in the top layer of the porous medium as a function of the particle Reynolds number  $Re_p$  defined in (3.4). The solid line is for  $\beta = 0.303$  with  $H/a = 10$ ; the circles are the results for  $\beta = 0.303$  with  $H/a = 12$  and the crosses for  $\beta = 0.180$  with  $H/a = 10$ . The other symbols are for  $H/a = 8$ : triangles for  $\beta = 0.303$ , pluses for  $\beta = 0.287$  and asterisks for  $\beta = 0.246$ .

Beavers & Joseph based their relation (1.1) on the assumption that ‘the slip velocity for the free fluid is proportional to the shear rate at the permeable boundary’ and, in their view, the parameter  $\alpha$  ‘depends only on the properties of the fluid and the permeable material’. Thus, the condition (1.1) would be expected to depend on the permeability of the porous medium and the local conditions near the interface, irrespective of the nature of the flow. As a consequence, a comparison of the values of  $\alpha$  necessary to fit data for pressure-driven and shear-driven flow would provide a test of the validity of (1.1).

On the basis of the very limited information available at the time, we pointed out in our earlier study (Zhang & Prosperetti 2009) that comparison of our numerical results for pressure-driven flow with others available in the literature for shear-driven flow suggested a difference between the values of  $\alpha$  in the two cases. We now address this point on the basis of a more extensive set of numerical results.

For this purpose we carried out two types of simulations in addition to the pressure-driven flow described before:

- (a) We replaced the upper part of the porous medium shown in figure 1 by a no-slip boundary as in the Beavers–Joseph experiments;
- (b) We set the pressure gradient to 0 and considered the shear flow driven by moving the no-slip plane replacing the upper part of the porous medium.

The results for pressure-driven flow were fitted by a quadratic function as shown in figure 8, while those for shear flow were fitted by a linear profile. In both cases the fitting was done allowing for the presence of slip at the porous medium interface. This procedure permitted us to calculate  $dU/dz$  and  $U_i \equiv U(z=0)$  at the interface.

An example of the values of  $\alpha$  obtained in this way is shown figure 11 for  $\beta = 0.155$  in dependence of the interfacial Reynolds number  $Re_i = 2aU_i/\nu$  for different values

---

$\beta$	$\alpha_s^0$	$\alpha_p^0$	$\theta \times 10^3$
0.303	0.857	0.857	4.4
0.287	0.893	0.898	4.6
0.268	0.938	0.949	4.8
0.246	0.994	1.015	4.9
0.221	1.068	1.101	5.0
0.201	1.126	1.175	5.1
0.191	1.164	1.222	5.2
0.180	1.197	1.254	5.3
0.155	1.285	1.371	5.5

---

TABLE 3. Parameter values necessary to fit the present numerical results by the Beavers–Joseph relation (1.1) with  $\alpha$  given in (8.1).

---

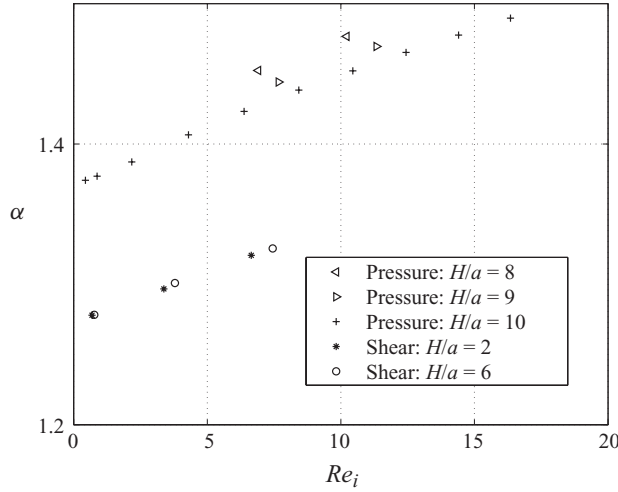


FIGURE 11. The values of  $\alpha$  needed to fit the Beavers–Joseph relation (1.1) to the numerical results for pressure-driven (upper set of symbols) and shear-driven flow. For pressure-driven flow, in ascending order, the symbols are for dimensionless channel heights  $H/a = 10, 9$  and  $8$ . For shear-driven flow, the asterisks and circles are for  $H/a = 2$  and  $6$ , respectively. The particle volume fraction is  $\beta = 0.155$ .

of the channel height. We comment on the effect of this parameter later. For the time being the point to note is that, evidently, the values of  $\alpha$  necessary to fit the shear-flow data, say  $\alpha_s$ , are about 10 % smaller than those necessary to fit the pressure-driven flow data,  $\alpha_p$ . Secondly, there is a clear Reynolds-number dependence which, at least in this parameter range, is very close to linear with the same slope in both cases. We have found a linear dependence in other cases as well and we can therefore write

$$\alpha_{s,p} = \alpha_{s,p}^0 (1 + \theta Re_i). \quad (8.1)$$

Numerical values for  $\alpha_s^0$ ,  $\alpha_p^0$  and  $\theta$  for several values of the volume fraction  $\beta$  are shown in table 3. An increase of  $\alpha$  with the Reynolds number was also found for flow over a bank of cylinders by Sahraoui & Kaviani (1992) for Reynolds numbers, based on the Darcy velocity, above 3. Due to the different geometry (cylinders versus spheres), their computed values of  $\alpha$  are significantly larger than the present ones and in line with what was found for cylinders in our earlier paper (Zhang & Prosperetti



2009). Thus, no quantitative comparison with the present results is possible. The same authors also found a difference between the values of  $\alpha$  for pressure-driven and shear flow, but they attributed it to inertial effects, which are essentially absent from our simulations at the lowest values of  $Re$  used and also from the (limited) results of Zhang & Prosperetti (2009).

It may also be noted that figure 4(a) of Sahraoui & Kaviany (1992) shows a drop of  $\alpha$  for Reynolds numbers beyond about 10. In this connection the authors observe: ‘The slip coefficient begins to decrease for Reynolds numbers larger than 10 because of the extrapolated shear at the interface. As shown in figure 3(c), for high Reynolds numbers the extrapolated velocity gradient underestimates the actual gradient, which results in a decrease in the slip coefficient. The slip coefficient without extrapolation increases monotonically for the range of Reynolds numbers shown in figure 4(a)’. We have not found any indication of a decrease of  $\alpha$  in the Reynolds number range we have investigated.

Even ignoring the Reynolds number dependence, which was negligible in the parameter range of Beavers & Joseph (1967), it would seem that the parameter  $\alpha$  has some dependence on the type of flow rather than being dependent ‘only on the properties of the fluid and the permeable material’ as postulated by these authors.

In order to examine this aspect more closely, let us use the Darcy relation (1.2) to re-cast the condition (1.1) in the form

$$U_i = \frac{1}{\mu} \left( \frac{\sqrt{\kappa}}{\alpha} \tau_i - \kappa \frac{dP}{dx} \right), \quad (8.2)$$

where  $\tau_i = \mu dU/dz$ . In this form, the relation may be interpreted as stating that the mean slip velocity  $U_i$  is driven by the combined effect of a shear, imposed by the flow in the channel, and of a pressure gradient. The length scale associated to the first effect is  $\sqrt{\kappa}/\alpha$ , while that associated to the second one is  $\sqrt{\kappa}$ .

It may be hypothesized that the Beavers–Joseph condition might be rendered less flow-dependent by allowing for the length scale of the pressure effect to differ from  $\sqrt{\kappa}$  writing, in place of (8.2),

$$U_i = \frac{1}{\mu} \left( \frac{\sqrt{\kappa}}{\alpha} \tau_i - \gamma \kappa \frac{dP}{dx} \right), \quad (8.3)$$

where the coefficient  $\gamma$  is presumably dependent on the volume fraction. With this modification we can retrace our steps backward from (8.3) to find, in place of (1.1),

$$\left. \frac{dU}{dz} \right|_{z=0} = \frac{\alpha}{\sqrt{\kappa}} (U_i - \gamma U_D). \quad (8.4)$$

An alternative justification of (8.4) from a very different point of view is provided in the Appendix. When the porosity is small  $U_D$  is very small and it will be effective only if  $\gamma$  is fairly large. When the porosity is significant, the difference from (1.1) can be appreciable also with a  $\gamma \sim O(1)$ .

Beavers & Joseph (1967) define a parameter  $\Phi$  expressing the increase in the flow rate with respect to that produced by the same pressure gradient in a plane no-slip channel. The same quantity is readily calculated from (8.4) with the result

$$\Phi = \frac{3(\sigma + 2\alpha\gamma)}{\sigma(1 + \alpha\sigma)}, \quad (8.5)$$

in which  $\sigma = H/\sqrt{\kappa}$ . Figure 12 shows the measured values of  $\Phi$  reported in figure 7 of Beavers & Joseph (1967) fitted using the two parameters  $\alpha$  and  $\gamma$ . The thin line

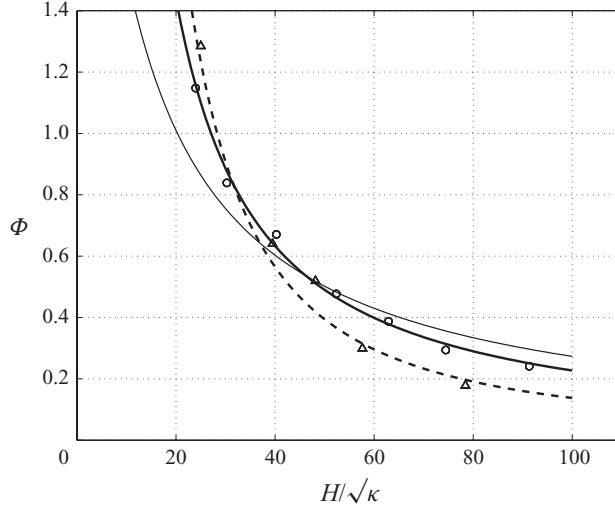


FIGURE 12. The data reported in figure 7 of Beavers & Joseph (1967) fitted using  $\alpha = 0.145$  and  $\gamma = 60$  for the porosity  $\kappa = 10^{-6} \text{ in.}^2$  ( $6.45 \times 10^{-4} \text{ mm}^2$ , circles) and  $\alpha = 0.4$  and  $\gamma = 110$  for  $\kappa = 2.48 \times 10^{-6} \text{ in.}^2$  ( $1.6 \times 10^{-3} \text{ mm}^2$ , triangles). The thin line is the original Beavers–Joseph fit with  $\alpha = 0.1$  and  $\gamma = 1$ . The quantity  $\Phi$  is the increase in the flow rate with respect to that produced by the same pressure gradient in a plane no-slip channel.

is the original Beavers–Joseph fit with  $\alpha = 0.1$  and  $\gamma = 1$ . The new fits are obtained with  $\alpha = 0.145$  and  $\gamma = 60$  for the porosity  $\kappa = 10^{-6} \text{ in.}^2$  ( $6.45 \times 10^{-4} \text{ mm}^2$ , circles) and  $\alpha = 0.4$  and  $\gamma = 110$  for  $\kappa = 2.48 \times 10^{-6} \text{ in.}^2$  ( $1.6 \times 10^{-3} \text{ mm}^2$ , triangles). It is obvious that the new fits improve on the original ones, especially at small values of  $H/\sqrt{\kappa}$ .

Several variants of the Beavers–Joseph condition have been proposed in the literature (see e.g. Alazmi & Vafai 2001 for a summary). Most of these alternative formulations equate the slip velocity to the difference between the two velocity gradients on the two sides of the interface (see e.g. Ochoa-Tapia & Whitaker 1995). Chandesris & Jamet (2009) also find a result of this type, but with the important feature that their procedure adds a term proportional to the pressure gradient. After using the velocity gradient on the porous medium side in terms of  $U_i$  and the Brinkman length scale, they end up with an equation that can be put in the form of (8.4) provided  $\alpha_s^0 = \sqrt{\beta}$ . The numerical data in table 3 are clearly at variance with this prescription.

Returning to the  $H$  dependence exhibited by the results of figure 11 (and also those of figure 10) we note that, for shear flow, the channel height becomes inconsequential for  $H/a$  as small as 2. The upper set of points in figure 11 is for pressure-driven flow between two porous media and  $H$  independence is achieved for  $H/a \simeq 10$ . By symmetry, for this type of flow one would expect height independence at twice the height for the shear flow, which is in reasonable agreement with the numerical results. Generally speaking, we find that the separation of scales necessary to justify an equivalent continuum description is not very marked, which should allay concerns expressed in the literature on the legitimacy of the Beavers–Joseph approach (see e.g. Auriault 2010).

For shear flow the modified relation (8.4) coincides with (1.1) and we therefore conclude that the parameter  $\alpha$  in (8.4) should be identified with  $\alpha_s$ . For pressure-driven flow, (1.1) gives a fit to the data with a different value of  $\alpha$ , namely  $\alpha_p$ . Thus,

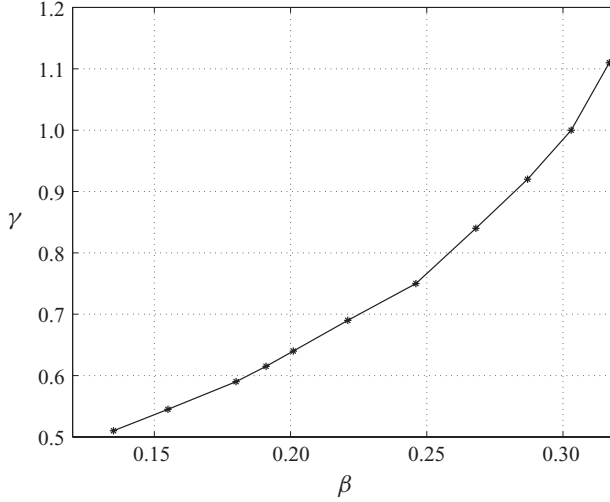


FIGURE 13. The new parameter  $\gamma$  appearing in the modified beavers–Joseph relation (8.2) as a function of the sphere volume fraction  $\beta$ .

the parameter  $\gamma$  should be adjusted in such a way that (1.1) and (8.4) give the same result for pressure-driven flow. Upon eliminating  $dU/dz$  between the two relations, we then find

$$\frac{\alpha_s}{\sqrt{\kappa}}(U_i - \gamma U_D) = \frac{\alpha_p}{\sqrt{\kappa}}(U_i - U_D), \quad (8.6)$$

from which

$$\gamma = \frac{\alpha_p}{\alpha_s} - \left( \frac{\alpha_p}{\alpha_s} - 1 \right) \frac{U_i}{U_D}. \quad (8.7)$$

Since, as mentioned before,  $\alpha_p$  and  $\alpha_s$  have the same dependence on the Reynolds number, the ratio  $\alpha_p/\alpha_s$  is independent of this quantity. When the Reynolds number is not too large, also  $U_i/U_D$  is approximately constant as can be seen, e.g., in figure 7, which then implies that  $\gamma$  is essentially independent of the interfacial Reynolds number. We have used relation (8.7) to calculate  $\gamma$  from the numerical simulations. The results are shown as a function of the sphere volume fraction in figure 13. The small irregularities in the curve are due to small errors in the fitting of the computed average velocity distributions.

The range of values of  $\gamma$  found here is different from that used in the fits of the Beavers–Joseph data in figure 12 and the trend with increasing porosity is also opposite. One reason for these differences might be the difference between the Darcy numbers in the two cases. If the Darcy number is estimated using the pore sizes quoted in Beavers & Joseph (1967) we find  $5.9 \times 10^{-3}$  and  $3.4 \times 10^{-3}$  for the two data sets reproduced in figure 12, to be compared with, e.g.  $\kappa/a^2 \simeq 6 \times 10^{-2}$  for our model porous medium with  $\beta = 0.303$ . It may be expected that, with a permeability smaller by 1 order of magnitude, the importance of the pressure gradient, i.e.  $U_D$ , needs to be considerably magnified to have a noticeable effect. The difference between the Darcy numbers is also responsible for the fact that the values of  $\alpha$  necessary to fit our results range between 0.8 and 1.3, as opposed to the value 0.1 used by Beavers & Joseph (1967). Another possible reason is the different structure of aloxite, described by Beavers & Joseph as ‘made from fused crystalline aluminum oxide grains held together with a ceramic bond’, and the model porous medium used in our simulations.

## 9. Conclusions

We have presented a numerical study of the flow in a channel bounded by one or two porous media modelled by cubic sphere arrays as sketched in figure 1. We have defined a slip velocity at the interface between the channel and the porous medium as the velocity averaged over a plane tangent to the spheres and we have examined to what extent this quantity can be modelled by the phenomenological relation (1.1). By comparing the results obtained for pressure-driven and shear-driven flow, we have found that the slip coefficient in the original form proposed by Beavers & Joseph (1967) depends somewhat on the nature of the flow. A modification of the relation is suggested to deal with this feature, and it is shown that the original Beavers–Joseph data are fitted by this modified relation better than by the original one. The modification is based on a physical argument and is supported by an independent derivation provided in the Appendix. The slip coefficient, in both the original and modified forms, was found to increase linearly with the particle Reynolds number.

The availability of a detailed Navier–Stokes solution for this situation has also permitted us to investigate the detailed nature of the flow and its dependence on the Reynolds number. Among other results, we have demonstrated the existence of a lift force on the particles facing the unobstructed channel flow which may contribute to the mobilization of bottom sediments. In order to determine whether this force is sufficiently large to be the dominant cause of particle lift-off, we can equate it to the apparent weight of a sphere of density  $\rho_p$  in a fluid of density  $\rho$ . Upon substituting the result in the expression of the so-called Shields number  $Sh$

$$Sh = \frac{\tau_i}{2a(\rho_p - \rho)g}, \quad (9.1)$$

and estimating the mean wall shear stress  $\tau_i$  from the relation  $\tau_i = -(H/2) dP/dx = \frac{1}{2} H \rho G$  valid for two-dimensional channel flow, we find

$$Sh = \frac{2}{3} \frac{F_z}{F_*}. \quad (9.2)$$

For the case of figure 9 the maximum value of  $F_z/F_*$  is about 0.4, which would give  $Sh \simeq 1.7$ , a value an order of magnitude larger than that usually accepted (see e.g. Lobkowsy *et al.* 2008; Ouriemi *et al.* 2009). It is therefore evident that this lift force by itself is insufficient to cause the particle lift-off, although it will contribute to it.

This work was completed while the senior author (A.P.) was a guest of the Institut Jean Le Rond d'Alembert of the Université Pierre et Marie Curie in Paris. He expresses his gratitude to the Director and the personnel of the Institute for their kind hospitality. This study was supported by National Science Foundation under grants CBET-0625138 and CBET-0754344.

## Appendix

### An alternative derivation of (8.4)

DANIEL LHUILLIER

Institut Jean Le Rond d'Alembert, CNRS (UMR 7190) and UPMC (Univ Paris 6),  
BC 162, 4 place Jussieu, F-75252 Paris Cedex 05, France

Porous media exhibit strong inhomogeneities close to their surface and these inhomogeneities are not easily amenable to a mathematical description. However,

let us assume (Goyeau *et al.* 2003) that a possible description is provided by a generalized Darcy–Brinkman equation. For a porous medium occupying the half-space  $z \leq 0$  exposed to a fluid flowing in the direction  $x$  (see figure 1) the flow is then described by

$$\mu \frac{\partial}{\partial z} \left( M(z) \frac{\partial U}{\partial z} \right) - \mu \frac{U(z)}{K(z)} - \frac{dP}{dx} = 0, \quad (\text{A } 1)$$

where  $U(z)$  is the averaged velocity defined in (6.3),  $P$  is the averaged fluid pressure and  $\mu$  is the fluid viscosity. The two functions of  $z$ ,  $M$  and  $K$ , introduced here are unknown except for their limit values,

$$M(0) = 1, \quad M(-\infty) \equiv m, \quad K(0) = \infty, \quad K(-\infty) = \kappa, \quad (\text{A } 2)$$

where  $\kappa$  and  $m$  are the permeability and the reduced viscosity of the (homogeneous) porous medium far from the surface  $z=0$ . The above Darcy–Brinkman equation is conveniently rewritten as

$$\frac{\partial}{\partial z} \left( M(z) \frac{\partial U}{\partial z} \right) = \frac{U(z)}{K(z)} - \frac{U_D}{\kappa}, \quad (\text{A } 3)$$

where  $U_D = U(-\infty)$  is the Darcy velocity. Integrating the above equation over the whole half-space and noticing that the velocity gradient vanishes far from the interface, one obtains

$$\left. \frac{\partial U}{\partial z} \right|_{z=0} = \int_{-\infty}^0 \frac{U(z) - U_D}{K(z)} dz - U_D \int_{-\infty}^0 \left( \frac{1}{\kappa} - \frac{1}{K(z)} \right) dz. \quad (\text{A } 4)$$

Note that this result is independent of the reduced viscosity  $m$ . An example of velocity profile is given in the left panel of figure 7 and it suggests that

$$U(z) - U_D = (U_i - U_D) f(z), \quad (\text{A } 5)$$

where  $U_i = U(0)$  is the mean fluid velocity at the porous medium surface, while  $f(z)$  decreases monotonically from  $f(0)=1$  to  $f(-\infty)=0$ . The behaviour of  $K(z)$  is less trivial because it cannot be taken for granted that it represents some non-homogeneous permeability. Nevertheless one can write

$$K(z) = \frac{\kappa}{1 - g(z)}, \quad (\text{A } 6)$$

with  $g(0)=1$  and  $g(-\infty)=0$  but the possibility of non-monotonic behaviour between these two limit values is to be kept in mind. With the profiles  $f(z)$  and  $g(z)$ , the velocity gradient at the surface is now given by

$$\left. \frac{\partial U}{\partial z} \right|_{z=0} = \frac{U_i - U_D}{\kappa} \int_{-\infty}^0 f(1 - g) dz - \frac{U_D}{\kappa} \int_{-\infty}^0 g dz. \quad (\text{A } 7)$$

And if one further assumes that the only length scale of the porous medium is  $\sqrt{\kappa}$  so that  $f$  and  $g$  depend on  $\tilde{z} = z/\sqrt{\kappa}$  only, then

$$\left. \frac{\partial U}{\partial z} \right|_{z=0} = \frac{\alpha}{\sqrt{\kappa}} (U_i - U_D) - \frac{\zeta}{\sqrt{\kappa}} U_D, \quad (\text{A } 8)$$

with

$$\alpha = \int_{-\infty}^0 f(1 - g) d\tilde{z}, \quad \zeta = \int_{-\infty}^0 g d\tilde{z}. \quad (\text{A } 9)$$

The continuity of velocity and velocity gradient at the porous interface with the pure liquid means that the above result is equivalent to (8.4) with  $\gamma = 1 + \zeta/\alpha$ .

The coefficient  $\alpha$  can be deduced by measuring  $U_i$  in a shear-driven experiment for which

$$U_i = \frac{\sqrt{\kappa}}{\alpha} \frac{\partial U}{\partial z}. \quad (\text{A } 10)$$

Once  $\alpha$  is known the coefficient  $\zeta$  can be deduced by measuring  $U_i$  in a pressure-driven experiment. If the clear fluid has a symmetric configuration as in figure 8, the velocity gradient at the interface is  $\partial U/\partial z(0) = (H/2\mu) |dP/dx| = U_D H/2\kappa$  and one obtains

$$U_i = \left(1 + \frac{\zeta}{\alpha} + \frac{H}{2\alpha\sqrt{\kappa}}\right) \left(\frac{\kappa}{\mu} \left|\frac{dP}{dx}\right|\right). \quad (\text{A } 11)$$

The linear dependence of the slip velocity on the gap  $H$  and the pressure gradient is to be noticed. If the configuration of the clear fluid involves a no-slip boundary at a distance  $H$  from the porous surface, as in Beavers & Joseph (1967), the slip velocity is given by

$$U_i = \frac{\alpha + \zeta + H/2\sqrt{\kappa}}{\alpha + \sqrt{\kappa}/H} \left(\frac{\kappa}{\mu} \left|\frac{dP}{dx}\right|\right) \quad (\text{A } 12)$$

and its dependence on  $H$  is more complicated than in the symmetric configuration. A direct consequence of this result is (8.5).

## REFERENCES

- ALAZMI, B. & VAFAI, K. 2001 Analysis of fluid flow and heat transfer interfacial conditions between a porous medium and a fluid layer. *Intl J. Heat Mass Transfer* **44**, 1735–1749.
- AURIAULT, J.-L. 1991 Heterogeneous medium. Is an equivalent description possible? *Intl J. Engng Sci.* **29**, 785–795.
- AURIAULT, J.-L. 2010 About the Beavers and Joseph boundary condition. *Transp. Porous Med.* **83**, 257–266.
- BAGCHI, P. & BALACHANDAR, S. 2002 Effect of free rotation on the motion of a solid sphere in linear shear flow at moderate Re. *Phys. Fluids* **14**, 2719–2737.
- BEAVERS, G. S. & JOSEPH, D. D. 1967 Boundary conditions at a naturally permeable wall. *J. Fluid Mech.* **30**, 197–207.
- BREUGEM, W., BOERSMA, B. & UITTENBOGAARD, R. 2005 The laminar boundary layer over a permeable wall. *Transp. Porous Med.* **59**, 267–300.
- CHANDESIS, M. & JAMET, D. 2009 Jump conditions and surface-excess quantities at a fluid/porous interface: A multi-scale approach. *Transp. Porous Med.* **78**, 419–438.
- CIESZKO, M. & KUBIK, J. 1999 Derivation of matching conditions at the contact surface between fluid-saturated porous solid and bulk fluid. *Transp. Porous Med.* **34**, 319–336.
- FURMAN, A. 2008 Modeling coupled surface-subsurface flow processes: A review. *Vadose Zone J.* **7**, 741–756.
- GHISALBERTI, M. 2009 Obstructed shear flows: similarities across systems and scales. *J. Fluid Mech.* **641**, 51–61.
- GOHARZADEH, A., KHALILI, A. & JØRGENSEN, B. B. 2005 Transition layer thickness at a fluid-porous interface. *Phys. Fluids* **17**, 057102.
- GOYEAU, B., LHUILLIER, D., GOBIN, D. & VELARDE, M. G. 2003 Momentum transport at a fluid-porous interface. *Intl J. Heat Mass Transfer* **46**, 4071–4081.
- HANSPAL, N. S., WAGHODE, A. N., NASSEHI, V. & WAKEMAN, R. J. 2006 Numerical analysis of coupled Stokes/Darcy flows in industrial filtrations. *Transp. Porous Med.* **64**, 73–101.

- JÄGER, W. & MIKELIC, A. 2009 Modelling effective interface laws for transport phenomena between an unconfined fluid and a porous medium using homogenization. *Transp. Porous Med.* **78**, 489–508.
- JAMES, D. & DAVIS, A. 2001 Flow at the interface of a fibrous porous medium. *J. Fluid Mech.* **426**, 47–72.
- KHAKPOUR, M. & VAFAI, K. 2008 Critical assessment of arterial transport models. *Intl J. Heat Mass Transfer* **51**, 807–822.
- KOPLIK, J., LEVINE, H. & ZEE, A. 1983 Viscosity renormalization in the Brinkman equation. *Phys. Fluids* **26**, 2864–2870.
- LARSON, R. E. & HIGDON, J. J. L. 1987 Microscopic flow near the surface of two-dimensional porous media. Part 2. Transverse flow. *J. Fluid Mech.* **178**, 119–136.
- LE BARS, M. & WORSTER, M. G. 2006 Interfacial conditions between a pure fluid and a porous medium: implications for binary alloy solidification. *J. Fluid Mech.* **550**, 149–173.
- LIN, C. J., PEERY, J. H. & SCHOWALTER, W. R. 1970 Simple shear flow round a rigid sphere: inertial effects and suspension rheology. *J. Fluid Mech.* **44**, 1–17.
- LIU, Q. & PROSPERETTI, A. 2010 Wall effects on a rotating sphere. *J. Fluid Mech.* **657**, 1–21.
- LOBKOWSY, A. E., ORPE, A. V., MOLLOY, R., KUDROLL, A. & ROTHMAN, D. H. 2008 Erosion of a granular bed driven by laminar fluid flow. *J. Fluid Mech.* **605**, 47–58.
- MARTYS, N., BENTZ, D. & GARBOCZI, E. 1994 Computer simulation study of the effective viscosity in Brinkman's equation. *Phys. Fluids* **6**, 1434–1439.
- MORAD, M. & KHALILI, A. 2009 Transition layer thickness in a fluid-porous medium of multi-sized spherical beads. *Exp. Fluids* **46**, 323–330.
- NEALE, G. & NADER, W. 1974 Practical significance of Brinkman's extension of Darcy's law: coupled parallel flows within a channel and a bounding porous medium. *Can. J. Chem. Engng* **52**, 475–478.
- NIELD, D. A. 2009 The Beavers-Joseph boundary condition and related matters: A historical and critical note. *Transp. Porous Med.* **78**, 537–540.
- NIELD, D. A. & KUZNETSOV, A. V. 2009 The effect of a transition layer between a fluid and a porous medium: shear flow in a channel. *Transp. Porous Med.* **78**, 477–487.
- OCHOA-TAPIA, J. & WHITAKER, S. 1995 Momentum transfer at the boundary between a porous medium and a homogeneous fluid i: theoretical development. *Intl J. Heat Mass Transfer* **38**, 2635–2646.
- OURIEMI, M., AUSSILLOUS, P. & GUZZELLI, E. 2009 Sediment dynamics. Part 1. Bed-load transport by laminar shearing flows. *J. Fluid Mech.* **636**, 295–319.
- POKRAJAC, D. & MANES, C. 2009 Velocity measurements of a free-surface turbulent flow penetrating a porous medium composed of uniform-size spheres. *Transp. Porous Med.* **78**, 367–383.
- POPOV, P., EFENDIEV, Y. & QIN, G. 2009 Multiscale modeling and simulations of flows in naturally fractured karst reservoirs. *Commun. Comput. Phys.* **6**, 162–184.
- RICHARDSON, S. 1971 A model for the boundary condition of a porous material. Part 2. *J. Fluid Mech.* **49**, 327–336.
- SAFFMAN, P. G. 1971 On the boundary condition at the surface of a porous medium. *Stud. Appl. Math.* **50**, 959–964.
- SAHRAOUI, M. & KAVIANY, M. 1992 Slip and no-slip velocity boundary conditions at interface of porous, plain media. *Intl J. Heat Mass Transfer* **35**, 927–943.
- SANGANI, A. & ACRIVOS, A. 1982 Slow flow through a periodic array of spheres. *Intl J. Multiphase Flow* **8**, 343–360.
- SEMINARA, G. 2010 Fluvial sedimentary patterns. *Annu. Rev. Fluid Mech.* **42**, 43–66.
- TAYLOR, G. I. 1971 A model for the boundary condition of a porous material. Part 1. *J. Fluid Mech.* **49**, 319–326.
- TILTON, N. & CORTELEZZI, L. 2008 Linear stability analysis of pressure-driven flows in channels with porous walls. *J. Fluid Mech.* **604**, 411–445.
- VAFAI, K. & KIM, S. 1990 Fluid mechanics of the interface region between a porous medium and a fluid layer - an exact solution. *Intl J. Heat Fluid Flow* **11**, 254–256.
- VALDÉS-PARADA, F. J., ALVAREZ-RAMIREZ, J., GOYEAU, B. & OCHOA-TAPIA, J. A. 2009 Computation of jump coefficients for momentum transfer between a porous medium and a fluid using a closed generalized transfer equation. *Transp. Porous Med.* **78**, 439–457.

- ZHANG, Q. & PROSPERETTI, A. 2009 Pressure-driven flow in a two-dimensional channel with porous walls. *J. Fluid Mech.* **631**, 1–21.
- ZHANG, Z. & PROSPERETTI, A. 2005 A method for three-dimensional particle flow simulations. *J. Comput. Phys.* **210**, 292–324.
- ZICK, A. A. & HOMSY, G. M. 1982 Stokes flow through periodic arrays of spheres. *J. Fluid Mech.* **115**, 13–26.